Nano Research

ISSN 1998-0124 CN 11-5974/O4
https://doi.org/10.1007/s12274-023-6025-z

Research Article

3D interlocked all-textile structured triboelectric pressure sensor for accurately measuring epidermal pulse waves in amphibious environments

Shaobo Si[1,§], Chenchen Sun[1,§], Yufen Wu[2], Jingjing Li[1], Han Wang[1], Yinggang Lin[1], Jin Yang[1] (✉), and Zhong Lin Wang[3,4] (✉)

[1] *Department of Optoelectronic Engineering, Key Laboratory of Optoelectronic Technology and Systems Ministry of Education, Chongqing University, Chongqing 400044, China*
[2] *College of Physics and Electronic Engineering, Chongqing Normal University, Chongqing 401331, China*
[3] *Beijing Institute of Nanoenergy and Nanosystems, Chinese Academy of Sciences, Beijing 100083, China*
[4] *School of Materials Science and Engineering, Georgia Institute of Technology, Atlanta, GA 30332, USA*
[§] *Shaobo Si and Chenchen Sun contributed equally to this work.*

Received: 9 May 2023 / **Revised:** 6 July 2023 / **Accepted:** 19 July 2023

ABSTRACT

The performance degradation and even damage of the e-textiles caused by sweat, water, or submersion during all-weather health monitoring are the main reasons that e-textiles have not been commercialized and routinized so far. Herein, we developed an amphibious, high-performance, air-permeable, and comfortable all-textile triboelectric sensor for continuous and precise measurement of epidermal pulse waves during full-day activities. Based on the principle of preparing gas by acid-base neutralization reaction, a one-piece preparation process of amphibious conductive yarn (ACY) with densely porous structures is proposed. An innovative three-dimensional (3D) interlocking fabric knitted from ACYs (0.6 mm in diameter) and polytetrafluoroethylene yarns exhibit high sensitivity (0.433 V·kPa^{-1}), wide bandwidth (up to 10 Hz), and stability (> 30,000 cycles). With these benefits, 98.8% agreement was achieved between wrist pulse waves acquired by the sensor and a high-precision laser vibrometer. Furthermore, the polytetrafluoroethylene yarn with good compression resilience provides sufficient mechanical support for the contact separation of the ACYs. Meanwhile, the unique skeletonized design of the 3D interlocking structure can effectively relieve the water pressure on the sensor surface to obtain stable and accurate pulse waves (underwater depth of 5 cm). This achievement represents an important step in improving the practicality of e-textiles and early diagnosis of cardiovascular diseases.

KEYWORDS

triboelectric pressure sensor, amphibious fabric, interlocking fabric, pulse wave measurement, one-piece preparation method

1 Introduction

Cardiovascular diseases (CVDs) remain the leading cause of human death. More than a quarter of the world's population is reported to suffer from CVD, contributing to nearly 20 million deaths per year globally [1, 2]. However, cardiovascular-associated mortality can be largely prevented through early monitoring and timely interventions [3]. Pulse waves contain extensive physiological and pathological information related to the cardiovascular system, and real-time continuous monitoring of pulse waves is important for the timely prevention and avoidance of serious diseases [4–11].

Textile-based wearable devices have shown unique potential in terms of wearable electronics due to their superior comfort and long-term wearability [12–18]. Recently, numerous textile-based sensors have been developed for the continuous monitoring of human physiological signals with great advances, including capacitive [19–22], resistive [23–26], and piezoelectric [27–32]. However, in practical scenarios, textile-based sensors applied to human surfaces are unavoidably exposed to various humidity environments, such as rain and sweat, even underwater, which seriously affects the usability and promotion of e-textiles in daily life. Therefore, it is imperative that e-textiles need to maintain excellent electrical and mechanical properties in both high-humidity and dry environments. Existing studies usually use coating, laminating, film stretching, and casting to laminate waterproof materials on the surface of fabrics/yarns to block water interference [33]. However, some common waterproof materials, such as silicone, polyurethane, and polydimethylsiloxane (PDMS), can restrict the degrees of freedom of the sensor structure, resulting in a decrease in the sensitivity of the sensor itself and not facilitating the sensing of weak pressure signal [34]. In addition, comfortable is also an important indicator for evaluating textile-based sensors. Materials commonly used to protect e-textiles from environmental moisture often limit their breathability, making them highly susceptible to human discomfort during long-term

Address correspondence to Zhong Lin Wang, zhong.wang@mse.gatech.edu; Jin Yang, yangjin@cqu.edu.cn

wear. Moreover, rigid substrates and thick textures often mean that these e-textiles do not fully comply with the complex concave contours of the wrist, which can lead to poor accuracy and instability of the pulse waves [19]. Although wearing a sensor too tightly on the wrist can capture stable pulse waves, excessive pressure can cause changes in the shape of the vessels, and the resulting obtained pulse waves do not accurately reflect the physiological conditions of the blood vessels. At present, this is a common problem with all types of pressure sensors.

Taking advantage of the abundant variety of textiles, an alternative technological path has been proposed [35]. Based on the principles of triboelectrification and electrostatic induction, textile substrates usually do not require additional or excessive modification processes, which not only reduces time as well as process costs but also ensures that textile-based sensors are better able to meet the demand for comfort. In addition, structural deformations caused by weak pressure need to be sensed only in terms of the difference in electronegativity between different textile materials, providing a richer structural design concept for achieving the accurate measurement of wrist pulse waves [15, 36–40]. Although textile-based triboelectric nanogenerators (TENGs) are equally susceptible to environmental humidity remain, the constraints of the waterproof layer on the flexibility of the sensor structure can be reduced by a reasonable choice of waterproof materials and preparation methods (Table S1 in the Electronic Supplementary Material (ESM)) [41–43]. Furthermore, based on the diversity of fabric structures, designing a reasonable fabric structure to improve the efficiency of inter-structural mechanical transfer to overcome the weakening of the performance by the waterproof material and thus achieve the purpose of enhancing the response of the sensor to weak pressure is also a worthwhile path to explore.

In this context, we report an air-permissible, comfortable, highly sensitive, and waterproof all-textile sensor (WATS) with a three-dimensional (3D) interlock structure for the accurate real-time measurement of pulse waves during full-day activities. The WATS exhibits high sensitivity (0.433 V·kPa^{-1}), a wide working frequency bandwidth (up to 10 Hz), and stability (> 30,000 cycles). Based on the principle of gas preparation by acid-base neutralization reaction, an economical and operable preparation process is proposed for the one-piece preparation of amphibious conductive yarn (ACY). The densely distributed porous structure within the ACY plays a key role in improving the pressure-sensing ability and sensitivity of the sensor. The used knitting polytetrafluoroethylene (PTFE) yarns with good compression resilience concentrate weak vibrations of the wrist pulse inside the ACY through the interlock structure, providing sufficient mechanical support for the contact–separation of its sheath–core structure. Moreover, the adopted skeletonized interlock structure further assists WATS in releasing a portion of the underwater pressure, ensuring the accuracy and stability of WATS in acquiring the wrist pulse signal underwater. Furthermore, with the guarantee that the internal flexibility of the interlocking structures is not compromised, fixing the above structure to the mesh nylon fabric into an array allows the sensor to maintain a consistent output over a wide range of curved surfaces at all times. In practice, the WATS can obtain accurate pulse waves for different types of wrist surfaces (flat, concave, and convex). The wave of the wrist pulse measured by this sensor is 98.8%, consistent with the displacement signal generated by laser vibrometry (displacement accuracy of 0.5 pm) of the pulse in the same position.

2 Results and discussion

2.1 Fabrication and design

To avoid the impact of the humid environment on sensor performance in the sensing process, we have proposed an ACY based on the triboelectric effect for realizing weak pressure sensing, as shown in Fig. 1(a). The ACYs adopt the classical sheath–core structure, with the conductive yarn as the electrode and triboelectric layer and the silicone layer as the waterproof shell as well as the triboelectric layer, which induces contact separation between the silicone layer and the conductive yarn under the action of external force to realize the force–electric conversion process. However, due to the fluidity of silicone before curing, the silicone on the surface of conductive yarn penetrates the yarn gap, resulting in too small a gap between the two triboelectric layers to ensure the contact–separation process. In this regard, we have attempted to ensure an effective contact separation space between the silicone waterproof layer and the conductive yarn by introducing a multi-porous structure between the two, and have proposed a new preparation method to realize the one-piece formation of ACYs with a multi-porous structure. The realization of this method is based on the acid-base neutralization reaction of H^+ in weak acids with HCO_3^- in $NaHCO_3$ to produce CO_2 gas, which forms finely porous structures in the silicone. As the silicone solidifies, fine porous etched structures are left and formed on the inner surface and inside of the silicone layer, respectively. The electron micrograph of the porous etched structure inside the silicone is shown in the inset of Fig. 1(b). Compared to conventional silicone elastomers, silicone with a multi-pore structure has better resilience, resulting in greater pressure sensing ability. The electron micrograph in Fig. 1(b) shows the cross-section of ACY with a similarly dense pore structure between the conductive yarn and the silicone layer. Based on the triboelectric effect, the multi-pore structure between the silicone layer and the conductive yarn further provides a larger contact area for the sensing process, which plays a key role in improving sensor sensitivity. This is important for the triboelectrification and electrostatic induction that can be generated by friction between materials inside the ACY alone. Moreover, the thickness of the silicone layer on the surface of the ACY is very thin, only 0.1 mm, which means its flexibility is not significantly different from that of the original conductive yarn (Fig. 1(c)). Notably, the economic and operational advantages of this one-piece waterproof yarn preparation method facilitate its further mass production and processing, and the described method of preparing porous structures has general applicability in the preparation of structural yarns of the same type.

To enhance the response of the sensor to subtle pressure signals, enabling it to be more effectively applied in the acquisition of human pulse waves, we designed a 3D interlocking structure as follows: Mesh nylon fabric serves as the base, and the ACY and PTFE yarn are sewn into each side of the mesh nylon fabric using a chain-lock stitch method, presenting the interlocking structure of two yarns on the surface of the mesh nylon yarn, as illustrated in Fig. 1(d). Moreover, the diameter of the ACY (0.6 mm) is larger than that of the PTFE yarn (0.4 mm) (Fig. S1 in the ESM). When the two yarns are knitted together with the same size of interlock stitch, the coils of the PTFE yarn are surrounded by the coils of the ACY, and there is a gap between the coils of the two yarns (Fig. S2 in the ESM), thus increasing the degree of freedom between the structures of the coils and providing higher sensitivity under dynamic pressure. The nylon mesh fabric, with its flexible structure and light texture, is used as the base and skeleton supporting the sensor structure. As shown in Fig. S3 in the ESM, a piece of nylon mesh fabric with a thickness of 40 nm has a size of 1 mm × 1 mm for each mesh. Its mesh structure not only increases the flexibility of the sensor but also provides a larger sensing area between the two yarns. Furthermore, the interlocking structures are arranged on the nylon mesh fabric in horizontal

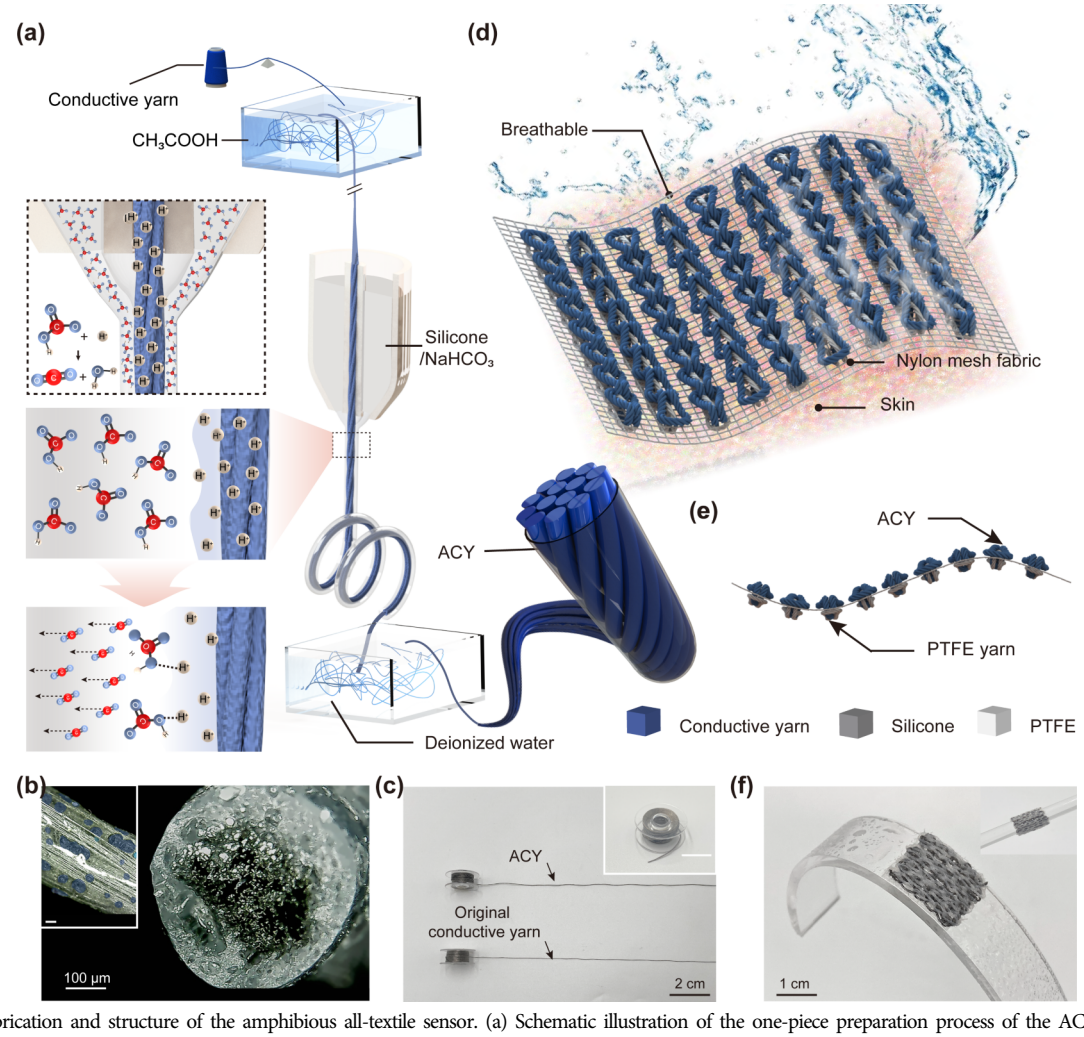

Figure 1 Fabrication and structure of the amphibious all-textile sensor. (a) Schematic illustration of the one-piece preparation process of the ACY with porous structure. (b) Electron micrograph of the cross-section of the ACY (scale bar, 100 μm). The inset shows the porous etched structure on the surface of silicone after the neutralization reaction of CH_3COOH solution with $NaHCO_3$-doped silicone to produce CO_2 (scale bar, 50 μm). (c) Photograph of the ACY and original conductive yarn. (d) Schematic illustration of the 3D interlocking structure of the WATS. (e) 3D interlocking structures arranged in an array on the nylon mesh fabric. (f) Photograph of the WATS in various degrees of bending.

arrays with each column independent of the others, which further enhances the flexibility of the overall structure of the sensor, as shown in Fig. 1(e). As a result, the WATS knitted from this ACY has the merits of being thin (1.36 mm) and lightweight (0.153 g at 2.0 cm × 2.0 cm) (Fig. S4 in the ESM). Its flexible structure also allows it to adapt to various deformations, as shown in Fig. 1(f).

2.2 Structure and working mechanism

To facilitate the analysis of the working principle of WATS, we took the example of the mechanical relationship between the units of an interlocking structure. The interlocking structure is formed by two yarns crossing each other and interweaving separately as they pass through opposite sides of the fabric (Fig. 2(a)). Except for the interlocking knot, the rest of the interlocking structure is in a relatively loose and highly free state. Therefore, the structure does not rely on additional external pressure and only needs to gently cover the wrist (Fig. 2(b)), and the force caused by the human pulse can cause contact separation between the two independent parts of the interlocking structure, as shown in Fig. 2(c). The process of contact between the PTFE yarn and ACY is also the process for force transfer. To improve the perception of the ACY for weak pressure, we carried out an acid-base neutralization reaction in the ACY to prepare a porous structure and performed finite element analysis (FEA) for the compression of conventional silicone elastomer and multi-porous silicone elastomer under the same external force using COMSOL software. Figure 2(d) shows that the silicone elastomer with a multi-porous structure (7.46 mm) has a larger deformation displacement under the same pressure compared with the conventional silicone elastomer (5.23 mm), which indicates that the silicone elastomer with a multi-porous structure can sense the pressure change more sensitively.

Furthermore, in the interlocking structure, the force between the PTFE and ACY is transferred via point-to-point contact. Combined with the good compression resilience of PTFE, the point-to-point contact further contributes to stress concentration, which enables the transfer of the force caused by the human pulse to the ACY. As shown in Fig. 2(e), the point-to-point contact between two yarns includes but is not limited to the following three types: (1) internal cross-contact, (2) synclastic contact, and (3) tangential contact. To intuitively understand the stress distribution in response to external force stimulus, we performed FEA under different external forces using COMSOL software, as respectively shown in Fig. 2(f) and Fig. S5 in the ESM. When the displacement of the PTFE yarn moving upward increased from only 0.3 to 0.7 mm, the stress at the contact point between the PTFE yarn and the ACY gradually increased from 0.4 to 2.3 kPa. Moreover, the contact modes of the two yarns at the contact points coincide with the three modes mentioned in Fig. 2(e), which further indicates that the PTFE yarn has an important role in force transfer and stress concentration.

The ultimate goal of the concentrated stress is to achieve the

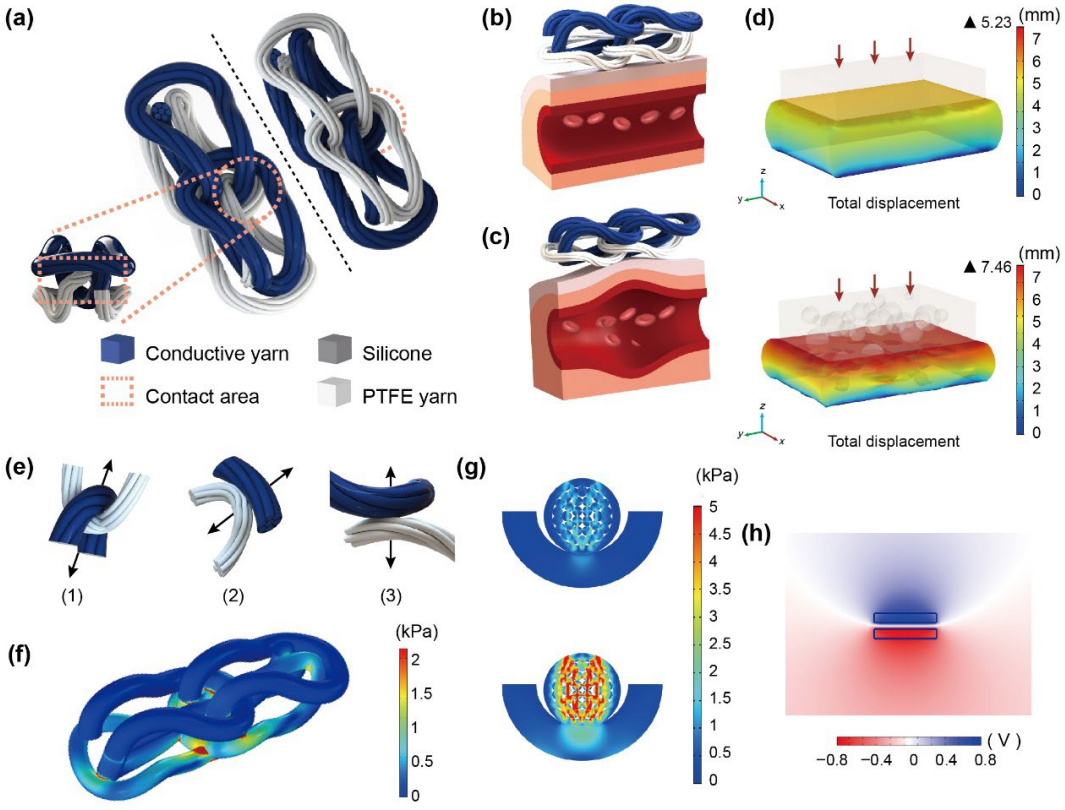

Figure 2 Working mechanism and electrical signal generation process. (a) Schematic illustration of the 3D interlocking structure of the WATS. (b) and (c) The working mechanism of the 3D interlocking structure in vibrations of the human pulse. (d) COMSOL was used to simulate the deformation displacement of conventional silicone elastomer and multi-porous silicone elastomer under the same applied pressure. (e) Contact manners between the PTFE yarn and the ACY in a coil: (1) internal cross-contact, (2) synclastic contact, and (3) tangential contact. (f) COMSOL was used to simulate the distribution of the 3D interlocking structure deformation under an applied pressure of 2.3 kPa. (g) COMSOL was used to simulate the distribution of the internal deformation of the ACY. (h) COMSOL was used to simulate the electrical potential distribution within the sensor under external pressure.

internal deformation of the ACY. The conductive yarn inside the ACY shown in Fig. 1(c) is in a loose and free state. There are also many gaps between the conductive yarn and silicone layer, and this structural feature makes the ACY more susceptible to deformation. To intuitively understand the stress distribution in response to external force stimulus, we performed FEA for the ACY containing three different diameters of single conductive yarns under different external forces using COMSOL software, as respectively shown in Fig. 2(g) and Fig. S6 in the ESM. As the displacement of the PTFE yarn moving upward increased from only 0.025 to 0.035 mm, the stress between the conductive yarns inside the ACY increased significantly, indicating that the internal structure of the ACY is capable of promoting considerable stress with very small displacement changes. Moreover, the smaller the diameter of the conductive yarn, the more evenly distributed the stress is among the conductive yarns inside the ACY, which is also more conducive to the deformation of the ACY inside. Therefore, the interlocking structure and the internal structural parameters of the ACY are of great importance for the sensor to be able to sensitively respond to the weak forces caused by the vibration of the human pulse.

The pulse pressure-induced periodical contact area change between the two yarns generates electrical signals through the combined effects of triboelectrification and electrostatic induction. The process of contact electrification can be effectively described by an electron cloud/potential model between silicone and Ag triboelectric layers, as shown in Fig. S7 in the ESM. When two atoms belonging to two different materials come into contact, induced by external periodical pulse pressure, the electron clouds overlap, and electrons transit from the Ag to the silicone. Accordingly, the electrical output of the textile triboelectric sensor is due to the electrostatic induction with a contact-separation operation model (Fig. S8 in the ESM). COMSOL simulation was employed to better visualize these distributions of surface charge potential, as shown in Fig. 2(h) and Fig. S9 in the ESM.

2.3 Electrical characterization of the WATS

A customized testing system was constructed to quantitatively characterize the output performance of the sensor (Fig. S10 in the ESM). To verify the effect of the PTFE knitting structure on the sensor performance, the relationship between the applied pressure and electrical output at a constant frequency of 1 Hz was obtained separately for sensors with and without the PTFE knitting structure (Fig. S11 in the ESM). When the applied pressure is between 0 and 0.25 kPa, the pressure sensitivity of the WATS with the PTFE knitting structure was almost six times higher than that of the sensor without the PTFE knitting structure. As the applied pressure increased to 1.5 kPa, the maximum output of the sensor without the PTFE knitting structure was only 0.086 V, while the output of the WATS with the PTFE knitting structure reached 0.363 V. In addition, by comparing the output waveform details of the two structures when receiving a constant pressure of 0.05, 0.5, and 1.0 kPa, respectively, it can be seen that the output waveforms of the WATS with the PTFE knitting structure remained consistent in both output amplitude and detail. However, the sensor without the PTFE knitting structure performed much less well in this regard, as shown in Fig. 3(a). The main reason for this difference is that the silicone on the surface of the ACY is elastic, and its knitting structure is loose, resulting in poor signal stability. The PTFE knitting structure can play an effective role in supporting the ACY structure, resulting in greater deformation of the waterproof yarn through stress concentration, leading to high

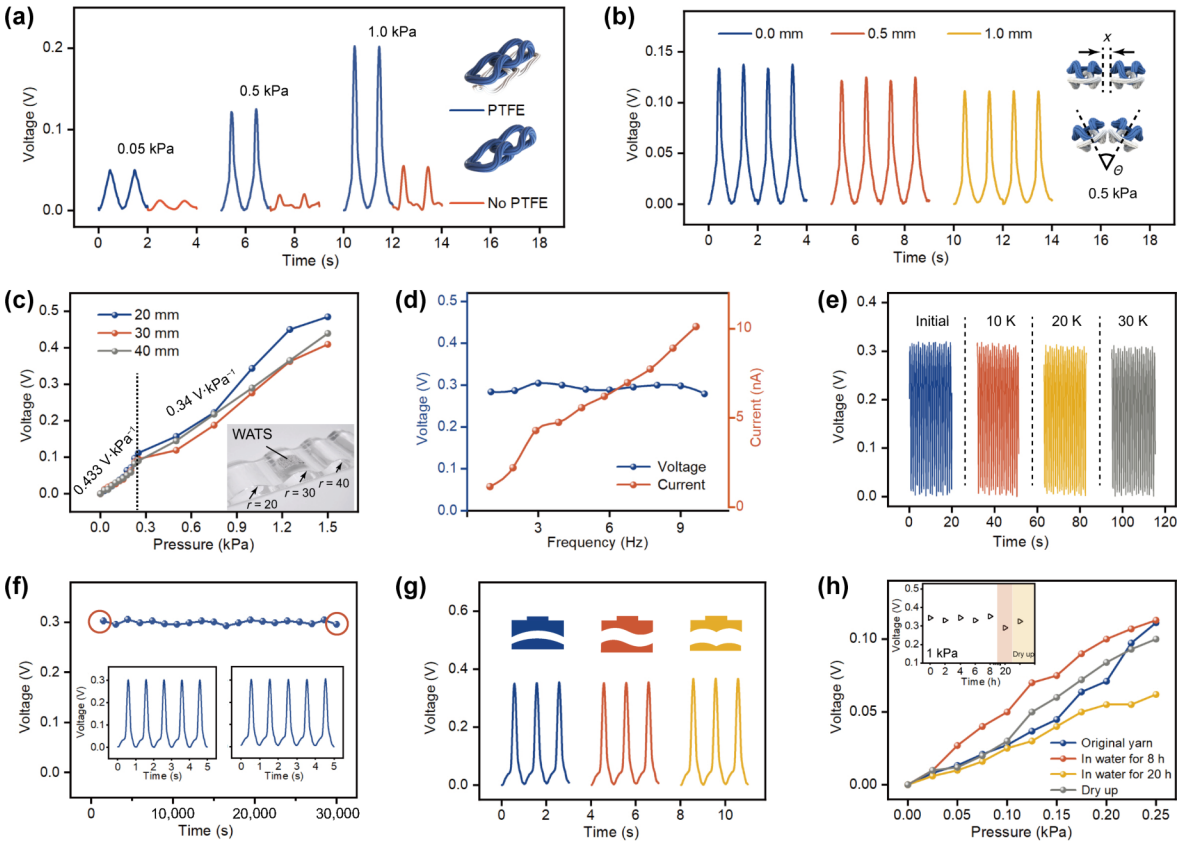

Figure 3 Electrical and mechanical characterization of the WATS. (a) Output voltage of WATS with and without the PTFE knitting structure under applied pressures of 0.05, 0.5, and 1 kPa, respectively. (b) Effect of the spacing x (0, 0.5, and 1.0 mm) of the array structure on the output voltage of the WATS under an applied pressure of 0.5 kPa. (c) Output voltage of the sensor at three bending radiuses (20, 30, and 40 mm). (d) Output voltage and current changes in the sensor under an applied pressure of 1 kPa with frequencies from 1 to 10 Hz. (e) Output voltage of the WATS under 30,000 pressing/releasing cycles. (f) Output voltage of the WATS after 30,000 stretching/releasing cycles. (g) Output voltage of the WATS on three morphological surfaces. (h) The effect of underwater immersion time on the output voltage of the WATS.

sensitivity. This is consistent with the simulation results shown in Fig. 2(f).

Typically, there is a prominent bone on the palm side, and the arterial blood vessels lie between the bone and the skin. Due to individual differences in the human body, the shape of bone and the thickness of fat directly affect the shapes of the arterial blood vessels in the wrist epidermis. The differences in human body wrist morphology comprise three categories—flat form, concave form, or convex form—as shown in Fig. S12 in the ESM. A lack of flatness of the wrist surface usually results in a gap between the sensor and the skin, which can affect the quality of the acquired signal or even mean that the sensor may fail to detect the human pulse. As a result, the 3D interlocking structures are arranged in horizontal arrays to ensure that the WATS can be used with a variety of wrist surface shapes to detect a high-quality pulse wave. There is a certain interval, x, between each column, which further ensures that each column can present a wide range of angles θ between the interlocking structure to accommodate the various radians of the wrist surface. We tested the voltage output of the sensors with different array intervals of x (0, 0.5, and 1.0 mm) on a surface with a curvature radius of 20 mm. Figure 3(b) and Fig. S13 in the ESM illustrate that the three intervals of x have little effect on their output. This may be due to the independent structure of the columns, which already provide the WATS with good flexibility.

To investigate the output performance of the WATS at different curvature radians, the sensor was placed on the surface with curvature radians of 20, 30, and 40 mm to obtain the relationship between the applied pressure and electrical output at a constant frequency of 1 Hz. The output voltage of the sensor had a consistent growth trend under different radiuses of curvature, as shown in Fig. 3(c) and Fig. S14 in the ESM. The curves for the voltage in response to the applied pressure exhibited two linear regions due to the different contact–separation area changes at different pressures—a quick increase in the low-pressure range and a slow increase in the high-pressure range. The sensitivity was 0.433 V·kPa^{-1} when the pressure was below 0.25 kPa. In the high-pressure range (> 0.25 kPa), the sensor exhibited a lower voltage sensitivity of 0.34 V·kPa^{-1}, attributed to the saturation of the effective contact–separation area.

Additionally, we examined the frequency response characteristics of the WATS. The results presented in Fig. 3(d) show that the sensor is capable of operating effectively within a range of 1 to 10 Hz under a constant pressure of 1 kPa, which adequately meets the need of physiological monitoring and diagnostic purposes. To ensure that the performance of the sensor does not deteriorate over a long period of continuous operation, we also tested the repeatability of the WATS for compression in the vertical direction and stretch in the horizontal direction, as shown in Figs. 3(e) and 3(f). Under the fixed applied pressure of 1 kPa, the output voltage showed no obvious discrepancy after more than 30,000 pressing cycles; the output performance also showed no significant change after more than 30,000 tensile cycles at a stretching force of 0.5 N. The results demonstrated excellent mechanical robustness for practical applications.

Considering the more complex wrist surface morphology that the WATS may encounter in practical scenarios, we further compared the output performance of the sensors on different types of curved surfaces. The three morphological surfaces, as shown in Fig. 3(g), and the experimental results indicated that the WATS maintained a stable electric output under various bending conditions. Furthermore, the chemical and physical properties of

the silicone itself were stable, so the output performance of the WATS remained relatively stable even after being fully immersed in water for more than 8 h, as shown in Fig. 3(h) and Fig. S15 in the ESM. When the sensor is immersed in water for more than 20 h, the ACY becomes soft, resulting in significantly decreased sensitivity of the sensor in the pressure range of 0–0.25 kPa. As soon as the sensor is completely dry, its sensitivity can be restored to the initial state. Based on the above performance advantages, we have attempted to apply the WATS to more complex practical scenarios for measuring human pulse waves.

2.4 Pulse wave monitoring and analysis

The systematic characterization of both the electrical and mechanical properties of the sensor showed that it can flexibly adapt to the complex human surface and offers significant advantages in obtaining the accuracy of human pulse wave shapes and monitoring waveform stability in real-time. To better verify the sensing performance of the sensor for pulse wave acquisition on a variety of wrist surfaces, we combined the WATS with a comfortable and adjustable strap. This not only allows for a comfortable fit but also ensures that the sensor better fits the wrist shape. Figures 4(a_1)–4(c_1) show morphological diagrams of different wrist surfaces (flat wrist, concave wrist, and convex wrist all from healthy individuals), and the three characteristic points are all accurately captured (Figs. 4(a_2)–4(c_2)), including the peak of the advancing waves (P_1), the peak of the reflected waveforms (P_2), and the peak of the dicrotic waveforms (P_3) (Videos ESM1, ESM2, and ESM3). In addition, pulse waves can be converted to signals in the frequency domain by a fast Fourier transform, and the information contained in frequency domain signals can also reflect cardiovascular health status. The fundamental band in the spectrum represents the frequency of the heartbeat, which matches well with the heart rate gained from pulse waves in the time domain, as well as the more harmonic peaks and less noise, which help to define the health status of the cardiovascular system. As shown in the insets of Figs. 4(a_2)–4(c_2), several harmonic components were visible in the range of 0–10 Hz, indicating that the sensor can obtain the same good quality pulse wave on the wrist surface with different radians.

To ensure the accuracy of our WATS for the real-time measurement of human pulse, we measured the pulse waves at the same wrist pulse location using a laser vibrometer (OFV505/5000) with a displacement accuracy of 0.5 pm and the WATS, as shown in Fig. 4(d) and Fig. S16 in the ESM (Video ESM4). The consistency between the two sets of pulse waves was calculated at 98.8% (Fig. 4(e)). This indicated that our WATS has a high degree of accuracy.

Meanwhile, a commercial medical instrument (MHM-6000B) and the WATS were simultaneously utilized to measure pulse waves, as shown in Fig. 4(f) (Video ESM5). The photoelectric sensor probe of the commercial medical instrument was worn on the right index finger; the sensor was comfortably worn on the left

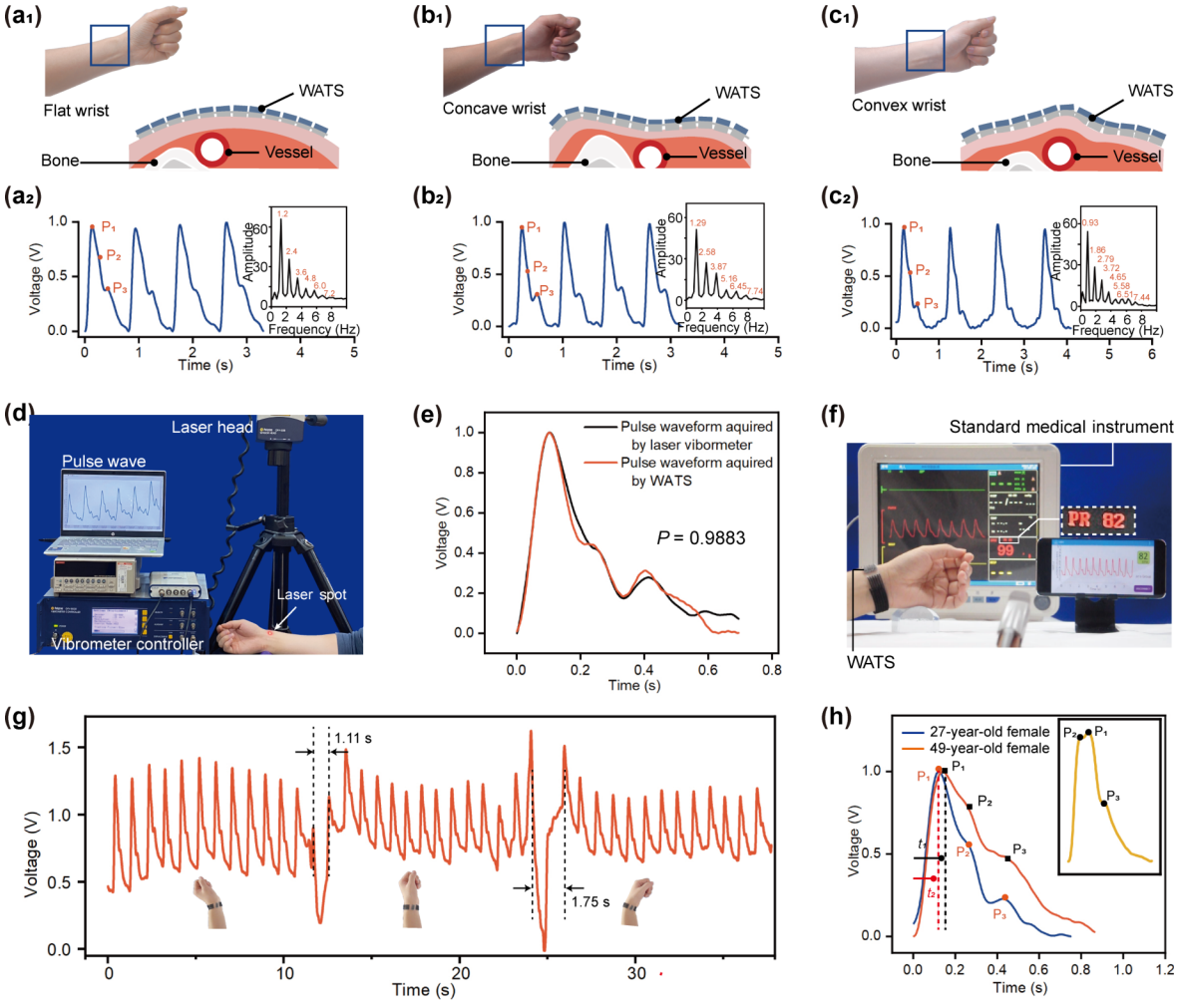

Figure 4 Pulse monitoring and analysis. (a_1)–(c_1) Schematic illustration of the three different forms of wrist types (flat, concave, and convex). (a_2)–(c_2) Analysis of pulse wave and frequency domain signals corresponding to three wrist types (flat, concave, and convex). (d) Measurement of the wrist pulse wave using a laser vibrometer (displacement accuracy of 0.5 pm). (e) Correlation coefficient between the pulse wave tested with laser vibrometry and the WATS. (f) Measurement of the pulse using the WATS and a standard medical device simultaneously. (g) Dynamic wrist pulse wave measurement. (h) Pulse waves of subjects of different ages. The inset shows the pulse wave of a hypertensive patient.

wrist. The results from the two measurements showed that the characteristic points in the fingertip pulse wave and wrist pulse wave were consistent, indicating that the sensor can measure the wrist pulse wave as accurately as the commercial instrument. Moreover, owing to the good sensitivity and large linear detection range of the sensor in a large pressure range, the pulse waves showed good stability in the dynamic monitoring upon wrist bending or moving; the corresponding pulse waves are presented in Fig. 4(g) (Video ESM6).

Based on the soft and flexible characteristics of the textile itself, its structure is usually subjected to different degrees of deformation by force pull and torsion, which can lead to the decline of the waveform mass obtained. To justify that the structure of the WATS can maintain long-term stability in pulse wave extraction, the acquired pulse waves after 5000 and 10,000 twisting cycles were also measured, respectively, as shown in Fig. S17 in the ESM. The shapes and characteristics of the pulse waves were almost consistent with the waveforms collected by the sensor in the initial state.

The universal applicability to different individuals is essential for the further promotion of the WATS; thus, we measured the wrist pulse waves of three participants (a 27-year-old healthy female, a 49-year-old healthy female, and an 83-year-old female who had arteriosclerosis), as shown in Fig. 4(h). The characteristic points of the pulse wave were successfully captured for all individuals. Since the oldest individual with atherosclerosis had poor arterial compliance, the pulse wave was spread through the arteries at a higher velocity, and the arrival time of the reflection waveform P_2 was advanced, as shown in the inset in Fig. 4(h).

We further obtained the pulse waves at the neck with greater surface curvature. As shown in Fig. S18 in the ESM, as the vibration of the human pulse at the neck is more intense, the characteristic points in the pulse wave are more obvious (Video ESM7). In terms of practical application, the WATS can be sewn into position in the collar of daily clothing to ensure the real-time monitoring of pulse waves. Then, we simultaneously collected two pulse waves at the neck and wrist positions of a participant (a 24-year-old healthy male). As shown in Fig. S19 in the ESM, the time difference between the peaks of the advancing wave (P_1) of the two pulse waves is the pulse transit time. We can calculate the pulse wave velocity (PWV) according to the equation. PWV = 795 $cm \cdot s^{-1}$, which is the characteristic value expected of a healthy adult.

2.5 WATS for measuring pulse waves underwater

Continuous lifelog data is imperative for identifying disease progression. WATSs in this paper provide important human physiological parameters for when a person is relaxing, exercising, swimming, bathing, and doing other activities throughout the day (Fig. 5(a)). These health data can be further uploaded to the cloud for big data analysis, and the treating doctor can simply download the data to make a timely diagnosis of the condition. To demonstrate the waterproofness of our WATS more adequately, we simulated a variety of life scenarios in our experiment.

First, to simulate the accidental wetting of the WATS surface by water, a sprayer was used to spray water onto the surface of the WATS on the wrist, and the wrist pulse wave was simultaneously acquired (Video ESM8). As shown in Fig. 5(b), the surface of the WATS is already covered in water droplets, and water droplets have even soaked the skin through the sensor. Comparing pulse waves collected before and after the sensor was sprayed with water, it can be seen that the water has little effect on the waveform amplitude, but the difference in waveform detail is not significant, as shown in Fig. 5(c) and Fig. S20 in the ESM. When the water was wiped off the surface of the sensor with a paper towel, the WATS was still relatively wet, but the output of the pulse wave was similar to that of the dry state.

Furthermore, we placed the WATS on the wrist while completely underwater to simulate the environment during bathing and swimming and to capture the pulse waves from the wrist (Figs. 5(d) and 5(e), and Video ESM9). In the experiment, we extended the wrist with WATS from its position in dry air into the underwater environment at a depth of 5 cm, continued to be immersed in water for a period of time and then moved to air; the pulse waves acquired continuously during this process are shown in Fig. 5(f). Due to the influence of underwater pressure and noise, when the WATS is deep underwater, the amplitude of the pulse wave is significantly reduced, and the overall waveform appears to fluctuate slightly. As the WATS was taken out of the water, the waveform amplitude was significantly improved and the overall waveform fluctuation was reduced, although the WATS was still wet. Then, by amplifying the pulse wave collected by the WATS in the above three states (Fig. 5(g)), it can be seen that the details of their time-domain signal waveforms differed; however, the time intervals between the characteristic points (P_1, P_2, and P_3) remained consistent. In particular, the skeletonization characteristics exhibited by the 3D Interlocking structure allow the WATS to mitigate some of the effects of water pressure, while the PTFE knitted structure with compressive resilience transmits the weak pulse pressure into the ACY, ensuring the accuracy of the collected pulse waveform. Moreover, the fundamental band and multiple harmonic components within 0–10 Hz could be clearly distinguished from their frequency domain signals (Fig. 5(h)). This indicates that the WATS can obtain the same high-quality pulse waves in both dry and underwater environments.

Finally, the pulse waves were obtained before and after a long period of vigorous human exercise. As a large amount of sweat is generated on the surface of the skin after strenuous exercise, the sweat also adheres to the knitted structure of the sensor, and the composition of the sweat may have some effect on the waterproof layer. Figure S21 in the ESM presents the waveforms measured at three states (normal, immediately after 30 min of jogging, and 30 min after cooling down). The details of the waveforms are shown in Fig. S22 in the ESM. Although the sensor was drenched in sweat after strenuous exercise, the amplitude of the pulse wave measured just after exercise was not greatly affected. Benefiting from the excellent breathability of the knitting structure of the WATS, the sweat on the surface of the wrist is evaporated through the knitting structure without significantly affecting the quality of the pulse wave; its amplitude and contour gradually returned to the initial state with increasing rest time.

3 Conclusions

In this work, we present a waterproof all-textile 3D structured sensor for continuously accurate measurement of epidermal pulse waves. Based on the principle of preparing gas by acid-base neutralization reaction, a one-piece preparation process of ACYs with densely porous structures is proposed, and the dense porous structure in ACY plays a key role in improving the pressure sensing capability of the sensor. The special ACY with TENG as the mechanism utilizes the abundant voids between the waterproof layer and its internal conductive yarn to provide the contact separation motion required to achieve force–electric conversion. The PTFE yarn with good compression resilience concentrates the external force on the ACY in the interlocking structure, making it more sensitive to the weak vibrations of the human pulse. Given these features, we obtained accurate and stable human wrist pulse waves using WATS both in underwater environments (underwater depth of 5 cm) and in sweat. With

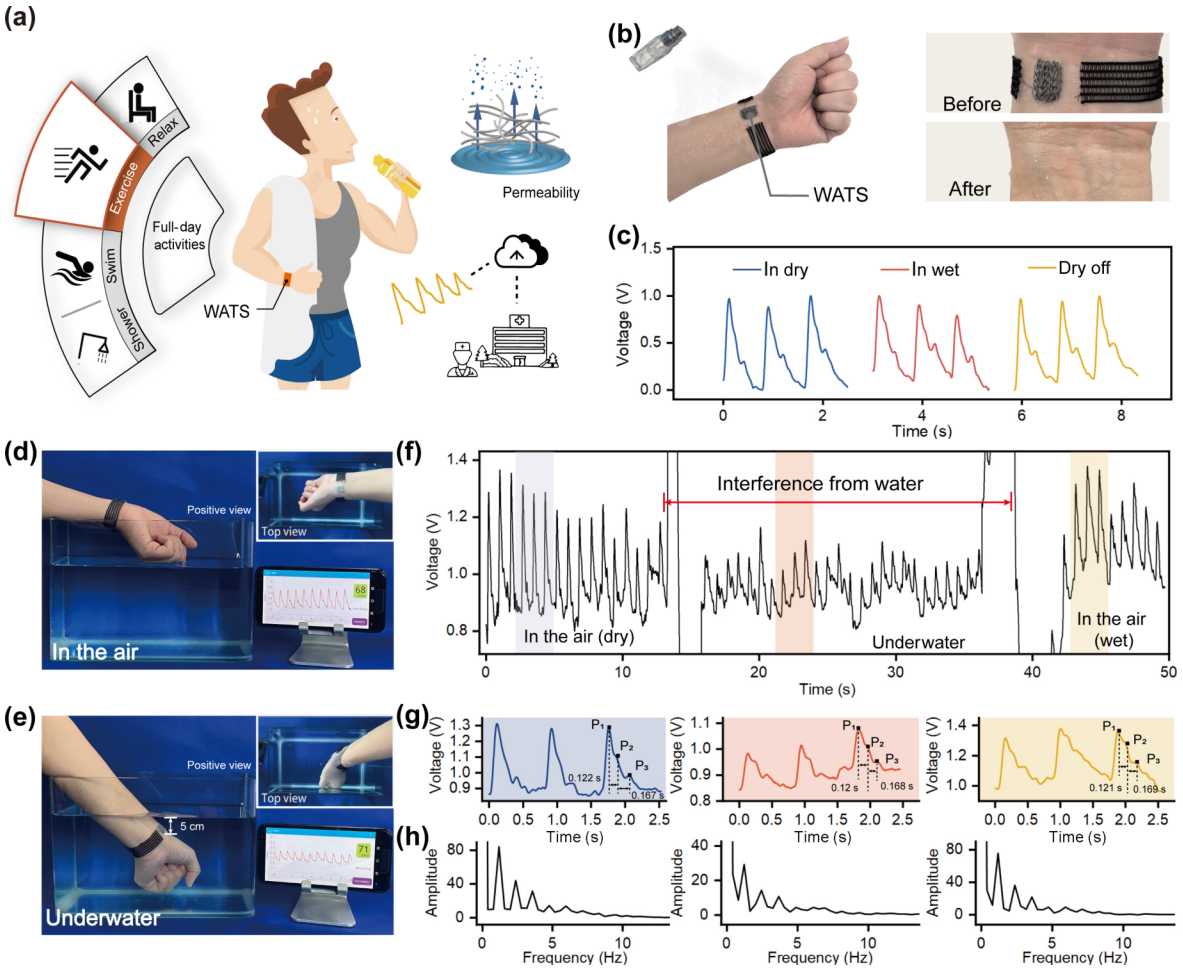

Figure 5 WATS for measuring pulse waves underwater. (a) WATS operates during full-day activities such as relaxing, exercising, swimming, and showering. The personal health data can be uploaded into the cloud, and doctors can download this data to make a preliminary diagnosis. (b) Photograph showing water droplets on the surface of the WATS and water droplets soaking the skin through the sensor. (c) Comparing the waveforms of the pulse signal collected before and after the WATS is sprayed with water. Photographs showing a WATS worn on the wrist (d) in the air and (e) underwater. (f) Continuous wrist pulse wave acquisition from dry air to underwater and out of water using WATS. Acquisition of (g) pulse time domain and (h) corresponding frequency domain signal waves from dry air to underwater and after exiting water using WATS.

excellent sensitivity (0.433 V·kPa^{-1}), wider working frequency bandwidth (up to 10 Hz), and stability (> 30,000 cycles), the pulse waves obtained by our WATS and laser vibrometer (displacement precision of 0.5 pm) were 98.8% consistent. Furthermore, the interlocking structure with high flexibility is independently fixed to the ultra-thin nylon mesh yarn in the form of an array so that it can show compatibility and comfort on complex curved wrist surfaces (flat, concave, and convex), even in dynamic flexion. This work presents an amphibious e-textile for improving their utility in daily life and making them useful for the early prevention and diagnosis of cardiovascular diseases.

4 Materials

Absolute CH_3COOH (99.5%) was purchased from Macklin Ltd. Absolute $NaHCO_3$ (AR) was supplied by Sinopharm Chemical Reagent Co., Ltd. Silicone rubber and curing agent were purchased from Macklin Ltd. (mixed at the weight ratio of 100:4), and the mixture was then degassed in a vacuum for 20 min. All chemicals were used directly without further purification.

5 Experimental

5.1 Fabrication of conductive yarn

The sliver-coated nylon yarn was made of nylon yarn with a diameter of 0.4 mm as the base. Under the protection of nitrogen, silver was coated on the surface of nylon yarn by an anion plating method, and then it was washed and dried.

5.2 One-piece preparation of amphibious yarn with porous structure

Firstly, the sliver-coated nylon conductive yarn was soaked in CH_3COOH solution with a concentration of 1.5%, and the silicone uniformly doped with $NaHCO_3$ powder was wrapped evenly on the surface of the conductive yarn through a self-designed device. Next, as the conductive yarn extended downward in the vertical direction, the $NaHCO_3$ in the silicone came into contact with the CH_3COOH on the surface of the conductive yarn, and an acid-base neutralization reaction occurred at the contact interface between the conductive yarn and silicone, producing CO_2 gas. Finally, under the action of the curing agent, silicone gradually solidified and the CO_2 suspended in silicone was stabilized, thus forming a fine pore structure.

5.3 Experimental setup for pressure and electrical characterization

A function generator (Stanford DS345) and an amplifier (LabworkPa-13) were employed to provide a sinusoidal pressure signal. A dual-range force sensor (Vernier Software & Technology, LLC.) was employed to measure the external pressure applied to the WATS. A Keithley system electrometer (Keithley 6514) was

utilized to monitor and record the output voltage and current of the WATS.

6 Use of the WATS

The measurements using WATS were performed with the consent of all volunteers who participated in the study. The WATS used in measurements will not have any bad effects on the volunteers.

Acknowledgments

This work was supported by the National Key Research and Development Project (No. 2021YFA1201600), the Natural Science Foundation Projects of Chongqing (No. cstc2022ycjh-bgzxm0206), and the Natural Science Foundation of Innovative Research Groups (No. cstc2020jcyj-cxttX0005).

Electronic Supplementary Material: Supplementary material (detailed Figs. S1–S22, Table S1, and Videos S1–S9) is available in the online version of this article at https://doi.org/10.1007/s12274-023-6025-z.

References

[1] Yusuf, S.; Wood, D.; Ralston, J.; Reddy, K. S. The world heart federation's vision for worldwide cardiovascular disease prevention. *Lancet* **2015**, *386*, 399–402.

[2] Nichols, W. W. Clinical measurement of arterial stiffness obtained from noninvasive pressure waveforms. *Am. J. Hypertens.* **2005**, *18*, 3–10.

[3] Vasan, R. S.; Larson, M. G.; Leip, E. P.; Evans, J. C.; O'Donnell, C. J.; Kannel, W. B.; Levy, D. Impact of high-normal blood pressure on the risk of cardiovascular disease. *N. Engl. J. Med.* **2001**, *345*, 1291–1297.

[4] Georgiopoulos, G.; Papaioannou, T. G.; Magkas, N.; Laina, A.; Mareti, A.; Georgiou, S.; Mavroeidis, I.; Samouilidou, E.; Delialis, D.; Tousoulis, D. et al. Age-dependent associations of carotid-to-femoral pulse wave velocity with coronary artery disease, cardiovascular risk and myocardial aging in high-risk patients. *J. Cardiovasc. Med.* **2019**, *20*, 201–209.

[5] Kallistratos, M. S.; Papanastasiou, A.; Bacalacou, K.; Zacharopoulou, I.; Kouremenos, N.; Kyfnidis, K.; Chamodraka, E.; Poulimenos, L. E.; Chiotelis, I.; Manolis, A. J. Screening for cardiovascular risk using pulse wave velocity. *Eur. Heart J.* **2013**, *34*, 3242.

[6] Cameron, J.; Dart, A. Pulse wave velocity as a marker of vascular disease. *Lancet* **1996**, *348*, 1586–1587.

[7] Ohkuma, T.; Ninomiya, T.; Tomiyama, H.; Kario, K.; Hoshide, S.; Kita, Y.; Inoguchi, T.; Maeda, Y.; Kohara, K.; Tabara, Y. et al. Brachial-ankle pulse wave velocity and the risk prediction of cardiovascular disease: An individual participant data meta-analysis. *Hypertension* **2017**, *69*, 1045–1052.

[8] Avolio, A. P.; Butlin, M.; Walsh, A. Arterial blood pressure measurement and pulse wave analysis—Their role in enhancing cardiovascular assessment. *Physiol. Meas.* **2010**, *31*, R1–R47.

[9] Meng, K. Y.; Chen, J.; Li, X. S.; Wu, Y. F.; Fan, W. J.; Zhou, Z. H.; He, Q.; Wang, X.; Fan, X.; Zhang, Y. X. et al. Flexible weaving constructed self-powered pressure sensor enabling continuous diagnosis of cardiovascular disease and measurement of cuffless blood pressure. *Adv. Funct. Mater.* **2019**, *29*, 1806388.

[10] Yang, J.; Chen, J.; Su, Y. J.; Jing, Q. S.; Li, Z. L.; Yi, F.; Wen, X. N.; Wang, Z. N.; Wang, Z. L. Eardrum-inspired active sensors for self-powered cardiovascular system characterization and throat-attached anti-interference voice recognition. *Adv. Mater.* **2015**, *27*, 1316–1326.

[11] Kim, D. H.; Ghaffari, R.; Lu, N. S.; Wang, S. D.; Lee, S. P.; Keum, H.; D'Angelo, R.; Klinker, L.; Su, Y. W.; Lu, C. F. et al. Electronic sensor and actuator webs for large-area complex geometry cardiac mapping and therapy. *Proc. Natl. Acad. Sci. USA.* **2012**, *109*, 19910–19915.

[12] Chen, G. R.; Li, Y. Z.; Bick, M.; Chen, J. Smart textiles for electricity generation. *Chem. Rev.* **2020**, *120*, 3668–3720.

[13] Fang, Y. S.; Zou, Y. J.; Xu, J.; Chen, G. R.; Zhou, Y. H.; Deng, W. L.; Zhao, X.; Roustaei, M.; Hsiai, T. K.; Chen, J. Ambulatory cardiovascular monitoring via a machine-learning-assisted textile triboelectric sensor. *Adv. Mater.* **2021**, *33*, 2104178.

[14] Meng, K. Y.; Zhao, S. L.; Zhou, Y. H.; Wu, Y. F.; Zhang, S. L.; He, Q.; Wang, X.; Zhou, Z. H.; Fan, W. J.; Tan, X. L. et al. A wireless textile-based sensor system for self-powered personalized health care. *Matter* **2020**, *2*, 896–907.

[15] Fan, W. J.; He, Q.; Meng, K. Y.; Tan, X. L.; Zhou, Z. H.; Zhang, G. Q.; Yang, J.; Wang, Z. L. Machine-knitted washable sensor array textile for precise epidermal physiological signal monitoring. *Sci. Adv.* **2020**, *6*, eaay2840.

[16] Chen, G. R.; Au, C.; Chen, J. Textile triboelectric nanogenerators for wearable pulse wave monitoring. *Trends Biotechnol.* **2021**, *39*, 1078–1092.

[17] Wen, D. L.; Pang, Y. X.; Huang, P.; Wang, Y. L.; Zhang, X. R.; Deng, H. T.; Zhang, X. S. Silk fibroin-based wearable all-fiber multifunctional sensor for smart clothing. *Adv. Fiber. Mater.* **2022**, *4*, 873–884.

[18] Wen, D. L.; Huang, P.; Li, B. Y.; Qiu, Y.; Wang, Y. L.; Zhang, X. R.; Deng, H. T.; Zhang, X. S. Silk fibroin/Ag nanowire-based multifunctional sensor for wearable self-powered wireless multi-sensing microsystems. *Nano Energy* **2023**, *113*, 108569.

[19] Lin, Q. P.; Huang, J.; Yang, J. L.; Huang, Y.; Zhang, Y. F.; Wang, Y. J.; Zhang, J. M.; Wang, Y.; Yuan, L. L.; Cai, M. K. et al. Highly sensitive flexible iontronic pressure sensor for fingertip pulse monitoring. *Adv. Health. Mater.* **2020**, *9*, 2001023.

[20] Park, H.; Kim, J. W.; Hong, S. Y.; Lee, G.; Lee, H.; Song, C.; Keum, K.; Jeong, Y. R.; Jin, S. W.; Kim, D. S. et al. Dynamically stretchable supercapacitor for powering an integrated biosensor in an all-in-one textile system. *ACS Nano* **2019**, *13*, 10469–10480.

[21] Atalay, A.; Sanchez, V.; Atalay, O.; Vogt, D. M.; Haufe, F.; Wood, R. J.; Walsh, C. J. Batch fabrication of customizable silicone-textile composite capacitive strain sensors for human motion tracking. *Adv. Mater. Technol.* **2017**, *2*, 1700136.

[22] Yang, Y.; Huang, Q. Y.; Niu, L. Y.; Wang, D. R.; Yan, C.; She, Y. Y.; Zheng, Z. J. Waterproof, ultrahigh areal-capacitance, wearable supercapacitor fabrics. *Adv. Mater.* **2017**, *29*, 1606679.

[23] Liu, M. M.; Pu, X.; Jiang, C. Y.; Liu, T.; Huang, X.; Chen, L. B.; Du, C. H.; Sun, J. M.; Hu, W. G.; Wang, Z. L. Large-area all-textile pressure sensors for monitoring human motion and physiological signals. *Adv. Mater.* **2017**, *29*, 1703700.

[24] Luo, N. Q.; Zhang, J.; Ding, X. R.; Zhou, Z. Q.; Zhang, Q.; Zhang, Y. T.; Chen, S. C.; Hu, J. L.; Zhao, N. Textile-enabled highly reproducible flexible pressure sensors for cardiovascular monitoring. *Adv. Mater. Technol.* **2018**, *3*, 1700222.

[25] Huang, T.; He, P.; Wang, R. R.; Yang, S. W.; Sun, J.; Xie, X. M.; Ding, G. Q. Porous fibers composed of polymer nanoball decorated graphene for wearable and highly sensitive strain sensors. *Adv. Funct. Mater.* **2019**, *29*, 1903732.

[26] Hu, X. R.; Huang, T.; Liu, Z. D.; Wang, G.; Chen, D.; Guo, Q. L.; Yang, S. W.; Jin, Z. W.; Lee, J. M.; Ding, G. Q. Conductive graphene-based E-textile for highly sensitive, breathable, and water-resistant multimodal gesture-distinguishable sensors. *J. Mater. Chem. A* **2020**, *8*, 14778–14787.

[27] Su, Y. J.; Chen, C. X.; Pan, H.; Yang, Y.; Chen, G. R.; Zhao, X.; Li, W. X.; Gong, Q. C.; Xie, G. Z.; Zhou, Y. H. et al. Muscle fibers inspired high-performance piezoelectric textiles for wearable physiological monitoring. *Adv. Funct. Mater.* **2021**, *31*, 2010962.

[28] Ahn, S.; Cho, Y.; Park, S.; Kim, J.; Sun, J. Z.; Ahn, D.; Lee, M.; Kim, D.; Kim, T.; Shin, H. et al. Wearable multimode sensors with amplified piezoelectricity due to the multi local strain using 3D textile structure for detecting human body signals. *Nano Energy.* **2020**, *74*, 104932.

[29] Mokhtari, F.; Spinks, G. M.; Fay, C.; Cheng, Z. X.; Raad, R.; Xi, J. T.; Foroughi, J. Wearable electronic textiles from nanostructured piezoelectric fibers. *Adv. Mater. Technol.* **2020**, *5*, 1900900.

[30] Mokhtari, F.; Cheng, Z. X.; Raad, R.; Xi, J. T.; Foroughi, J. Piezofibers to smart textiles: A review on recent advances and future

outlook for wearable technology. *J. Mater. Chem. A* **2020**, *8*, 9496–9522.

[31] Dai, Z.; Wang, N.; Yu, Y.; Lu, Y.; Jiang, L. L.; Zhang, D. A.; Wang, X. X.; Yan, X.; Long, Y. Z. One-step preparation of a core-spun Cu/P(VDF-TrFE) nanofibrous yarn for wearable smart textile to monitor human movement. *ACS Appl. Mater. Interfaces* **2021**, *13*, 44234–44242.

[32] Tan, Y. S.; Yang, K.; Wang, B.; Li, H.; Wang, L.; Wang, C. X. High-performance textile piezoelectric pressure sensor with novel structural hierarchy based on ZnO nanorods array for wearable application. *Nano Res.* **2021**, *14*, 3969–3976.

[33] Tehrani-Bagha, A. R. Waterproof breathable layers—A review. *Adv. Colloid Interface Sci.* **2019**, *268*, 114–135.

[34] de Medeiros, M. S.; Chanci, D.; Moreno, C.; Goswami, D.; Martinez, R. V. Waterproof, breathable, and antibacterial self-powered e-textiles based on omniphobic triboelectric nanogenerators. *Adv. Funct. Mater.* **2019**, *29*, 1904350.

[35] Zhang, C.; Bu, T. Z.; Zhao, J. Q.; Liu, G. X.; Yang, H.; Wang, Z. L. Tribotronics for active mechanosensation and self-powered microsystems. *Adv. Funct. Mater.* **2019**, *29*, 1808114.

[36] Lou, M. N.; Abdalla, I.; Zhu, M. M.; Wei, X. D.; Yu, J. Y.; Li, Z. L.; Ding, B. Highly wearable, breathable, and washable sensing textile for human motion and pulse monitoring. *ACS Appl. Mater. Interfaces* **2020**, *12*, 19965–19973.

[37] Wang, H.; Cheng, J.; Wang, Z. Z.; Ji, L. H.; Wang, Z. L. Triboelectric nanogenerators for human-health care. *Sci. Bull.* **2021**, *66*, 490–511.

[38] Nguyen, V.; Kelly, S.; Yang, R. S. Piezoelectric peptide-based nanogenerator enhanced by single-electrode triboelectric nanogenerator. *APL Mater.* **2017**, *5*, 074108.

[39] Zou, H. Y.; Zhang, Y.; Guo, L. T.; Wang, P. H.; He, X.; Dai, G. Z.; Zheng, H. W.; Chen, C. Y.; Wang, A. C.; Xu, C. et al. Quantifying the triboelectric series. *Nat. Commun.* **2019**, *10*, 1427.

[40] Dassanayaka, D. G.; Alves, T. M.; Wanasekara, N. D.; Dharmasena, I. G.; Ventura, J. Recent progresses in wearable triboelectric nanogenerators. *Adv. Funct. Mater.* **2022**, *32*, 2205438.

[41] Zhao, Z. Z.; Yan, C.; Liu, Z. X.; Fu, X. L.; Peng, L. M.; Hu, Y. F.; Zheng, Z. J. Machine-washable textile triboelectric nanogenerators for effective human respiratory monitoring through loom weaving of metallic yarns. *Adv. Mater.* **2016**, *28*, 10267–10274.

[42] Si, S. B.; Sun, C. C.; Qiu, J.; Liu, J.; Yang, J. Knitting integral conformal all-textile strain sensor with commercial apparel characteristics for smart textiles. *Appl. Mater. Today* **2022**, *27*, 101508.

[43] Cao, R.; Pu, X. J.; Du, X. Y.; Yang, W.; Wang, J. N.; Guo, H. Y.; Zhao, S. Y.; Yuan, Z. Q.; Zhang, C.; Li, C. J et al. Screen-printed washable electronic textiles as self-powered touch/gesture tribo-sensors for intelligent human–machine interaction. *ACS Nano* **2018**, *12*, 5190–5196.